



A Micromechanical Model for Simulation of Rock Failure Under High Strain Rate Loading

Mohammad Reza Majedi¹ · Mohammad Afrazi¹ · Ali Fakhimi^{1,2}

Received: 20 February 2020 / Revised: 6 June 2020 / Accepted: 13 July 2020 / Published online: 24 July 2020
© Iran University of Science and Technology 2020

Abstract

Quasi-brittle materials such as rock are rate sensitive materials and their behaviour under dynamic loading is not identical with that under static loading. In this study, numerical Brazilian tensile tests are conducted using a Split Hopkinson Pressure Bar system in an attempt to reproduce the dynamic increase factors (DIF) of the experimental tests. The rock is modelled by a bonded particle system made of spherical particles which interact at the contact points. The numerical results indicate that while the bonded particle system with a simple contact bond model can closely mimic the static behaviour of the sandstone specimens, it lacks what is needed for a rate dependent material. Therefore, a micromechanical model in which the contact bond strength is allowed to vary in proportion to the relative velocity of the involved particles is introduced. It is shown that the modified model can reproduce the physical tests data reported in the literature. In particular, with the application of strength enhancement coefficients in the range of $0-16 \times 10^5$, DIF values of 1.1–13 are obtained in the indirect tensile Brazilian tests, and the induced strain rate in the specimen is in $10-1000 \text{ s}^{-1}$ range. Our preliminary study indicates that the model, consistent with the fact reported for the quasi-brittle materials, shows different rate-dependent sensitivity and dynamic strength enhancement in tension and compression. The micromechanical parameters in the proposed model can be adjusted to reproduce the physical rock strength, and that the shape of the reflected and transmitted numerical waves can be modified to approach those in the physical tests.

Keywords Split Hopkinson Pressure Bar · Bonded particle system · Rock strength · Strength enhancement · Micromechanical model

1 Introduction

Materials subjected to high strain loading behave differently compared to the situation of static loading. This sensitivity of materials to the loading rate has created challenges and at the same time opportunities for deeper understanding of strength of materials. Rock blasting for

underground excavation, rock drilling, and strain burst of rock are examples of situations in which loading rate plays a role in dictating the material behaviour and the degree of rock fragmentation. Three main methods have been proposed for measuring rock strength under dynamic loading by the International Society for Rock Mechanics (ISRM). These proposed methods include compression test, Brazilian test, and Notched Semi-Circular Bend (NSCB) test. These tests are performed using the Split Hopkinson Pressure Bar (SHPB) to monitor the material behaviour, and measure the loading rate and material strength [1].

A comprehensive review of the SHPB testing of rock has been reported by Xia and Yao [2]. According to their review, John Hopkinson invented the SHPB testing technique in 1872 to investigate the propagation of stress waves along iron wires. Hopkinson's idea was modified a few times and, finally, Lindholm in 1964 was the person who

✉ Ali Fakhimi
A.fakhimi@modares.ac.ir

Mohammad Reza Majedi
M.majedi@modares.ac.ir

Mohammad Afrazi
Mohammad.afrazi@modares.ac.ir

¹ School of Civil and Environmental Engineering, Tarbiat Modares University, Tehran, Iran

² Department of Mineral Engineering, New Mexico Institute of Mining and Technology, Socorro, NM 87801, USA

suggested a testing set up which looks like the system as today's apparatus [3].

Since the invention of the SHPB apparatus, it has been used extensively to measure material strength under different loading rates. By conducting experimental splitting-tension tests, Hughes et al. [4] concluded that there is a shift of crack initiation time relative to the peak stress. Furthermore, experimental strength versus strain rate data indicates that the dynamic tensile strength of concrete is much higher than the static tensile strength. Dai et al. [5] used SHPB system to measure dynamic compressive and tensile strength of rocks, and to investigate the effect of slenderness of the compressive specimen and friction between the sample and bars on the measured results. Das [6] conducted experimental SHPB tests and presented a rate-dependent constitutive model to predict dynamic behaviour of sandstone under tensile loading. Li et al. [7] performed a set of SHPB experimental tests to study the explosion resistance of high-damping rubber materials. Crack propagation in coal specimens was investigated by Ai et al. [8]. In their work, Brazilian disk coal specimens with vertical and horizontal bedding were studied using the SHPB system. Experimental results suggest that the bedding direction has a major influence on the dynamic mechanical properties such as dynamic tensile strength and strain energy. The path of crack propagation is affected by the bedding plane direction, as well. Feng et al. [9] conducted SHPB tests to study the effect of strain rates on the dynamic flexural properties of rubber concrete. Their results show that adding rubber to the concrete makes the material more flexible and that the crack propagation speed is reduced.

Different constitutive models have been implemented and numerous numerical studies have been performed to investigate the failure and fracture behaviour of brittle materials such as rock and concrete in dynamic loading. Numerical methods including Finite Element Method (FEM), Discrete Element Method (DEM), and hybrid Finite Element and Discrete Element Method (FDEM) have been utilized for the mechanical simulation in the literature. Hughes et al. [4] conducted a comprehensive numerical splitting tensile analysis to investigate the effect of varying the uniaxial tensile strength of concrete on the crack initiation time, stress state, crack growth characteristics, and failure mode. Gálvez et al. [10] used FEM to model the SHPB testing system and to study tensile strength of ceramic materials at high rates of strain. Tedesco et al. [11] used FEM to study direct tension tests of plain concrete in a SHPB system. Their numerical analyses revealed the dynamic states of stress in the specimen prior to failure as well as the mode of failure. Meng and Li [12] investigated the uniformity of axial and radial stress in a specimen under uniaxial compressive loading using the finite-element method. In their work, the

role of specimen size and end friction on the stress distribution in the specimen was studied. Zhong et al. [13] investigated the influence of interface friction and specimen configuration on the material dynamic response using SHPB and nonlinear FE analysis.

Discrete element method (DEM) is a powerful technique in numerical modelling of geomaterials [14–16]. Cundall [17] developed DEM to simulate the interaction of blocks in a rock mass. Since then, the technique has been employed in the simulation of many geotechnical problems including rock cutting [18, 19], fracture process zone [20], rock spalling [21], rock blasting [22], and rock fracturing [23]. Brara et al. [24] used DEM to study the concrete material tensile behaviour at high strain. Particle Flow Code (PFC) was used by Li et al. [25] to study the effect of impact velocity on the compressive strength of rock. Yin et al. [26] used DEM to study mode I fracture toughness of granite in an SHPB test under different temperature conditions. The results show that DEM is capable of reflecting the mechanical properties of rocks at elevated temperatures. Du et al. [27] used DEM simulation to describe the failure behaviour of hydrostatically confined oblique cylindrical rock specimens under combined compression-shear loading in SHPB test. They investigated the effect of confining pressure and loading rate on the failure mechanism of rock.

Due to rock heterogeneity, the applicability of continuum based models to address rock engineering problems, particularly those that involve dynamic failure of rock, is limited [28]. Munjiza [29] formalized the idea of using a new hybrid finite-discrete element method (FDEM). In the FDEM, each discrete element is discretized into finite elements. In the context of the combined finite-discrete element method, transition from continua to discontinua is done through fracture and fragmentation processes [29]. Rougier et al. [30] used a 3D FDEM to model SHPB experiments on granite material and tried to reproduce the softening behaviour of the specimen. Osthus et al. [31] also used FDEM to simulate the SHPB test. Their work demonstrates good agreement between the FDEM and SHPB experimental tests results.

SHPB test can be simulated using a hybrid-bonded particle-finite element system. In this method, the incident and transmission bars are modelled by finite element, while the brittle material is simulated with a bonded particle system. Bonded Particle Method (BPM) is a simple version of discrete element technique in which the discrete particles are circular in 2D and spherical in 3D [32]. This technique was introduced by Cundall and Strack [33] in their pioneer work in the simulation of soil shear deformation. Fakhimi et al. [34] used the hybrid finite element-bonded particle system to simulate the SHPB test and to evaluate the strength characteristics of sandstone under uniaxial compressive loading. Their work revealed that the experimental strength enhancement cannot be successfully

captured if only the inertia of the tested material is considered. For this reason, a micromechanical model was proposed in their work which was capable of reproducing the dynamic results in the SHPB test.

In this study, the CA3 [35] computer program, which is a hybrid-bonded particle-finite-element 3D program, is used to simulate the Brazilian tensile test in an SHPB system. The micromechanical model proposed in [34] is utilized to examine the validity of the model in capturing strength enhancement in tensile failure of rock. The numerical results are presented and compared with the physical tests data reported in the literature.

2 Theoretical Background

A sketch of the SHPB apparatus is shown in Fig. 1. The test begins by shooting the striker bar using a gas gun. The striker bar impacts the incident bar, and as a result, the incident wave is generated. When the incident wave reaches the specimen, it decomposed into the reflected wave and transmitted wave. The combination of incident and reflected waves on one end and transmitted wave on the other end of the specimen causes severe damage to the rock specimen. Through the strain gages installed on the incident and transmission bars, the necessary information about the applied stress on the specimen and the loading rate can be obtained. The length of incident and transmission bars has to be long enough, so that the wave which is propagated along them can be assumed one dimensional.

Based on the one-dimensional wave equation for a given point along each of the bars, the strain is given by:

$$\begin{aligned} \epsilon_I &= -\frac{1}{c} \dot{u}_I \\ \epsilon_R &= \frac{1}{c} \dot{u}_R \\ \epsilon_T &= -\frac{1}{c} \dot{u}_T \end{aligned} \tag{1}$$

where ϵ is the strain, \dot{u} is the particle velocity, and the subscripts I, R, and T stand for incident, reflected, and

transmission bars, respectively. The elastic wave speed along the steel bars can be obtain from the following equation:

$$c = \sqrt{\frac{E}{\rho}} \tag{2}$$

In Eq. (2), E is the Young’s modulus and ρ is the density of the bars.

As shown in Fig. 2, in the case of dynamic equilibrium, the summation of incident and reflected strains (ϵ_I, ϵ_R) must be equal to the transmitted strain (ϵ_T) [34]. This ensures that the forces (F_a, F_b) at the two ends of the specimen (points a and b in Fig. 2) are equal. Therefore, we have:

$$(\epsilon_I + \epsilon_R)_a = (\epsilon_T)_b \tag{3}$$

If the above condition of dynamic equilibrium is satisfied, tensile stress (σ_τ) at the center of the Brazilian specimen can be calculated by the following equation (Fig. 3):

$$\sigma_\tau = \frac{2p(\tau)}{\pi Dt} \tag{4}$$

In Eq. (4), τ is the time, D and t are the diameter and thickness of the disk, and $p(\tau)$ is the applied load to the specimen which is given by:

$$p(\tau) = \frac{F_a + F_b}{2} = \frac{EA}{2} (\epsilon_I + \epsilon_R + \epsilon_T) \tag{5a}$$

Using Eq. (3), Eq. (5a) can be simplified as:

$$p(\tau) = EA\epsilon_T \tag{5b}$$

Hughes et al. [4] estimated stress rate ($\dot{\sigma}$) and strain rate ($\dot{\epsilon}$) from the following equations:

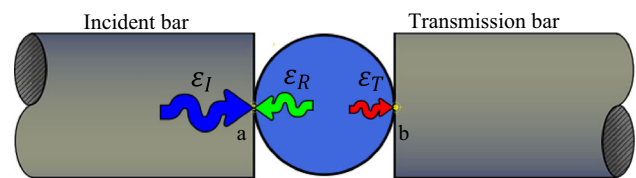


Fig. 2 Strains of the bars at the two sides of the specimen

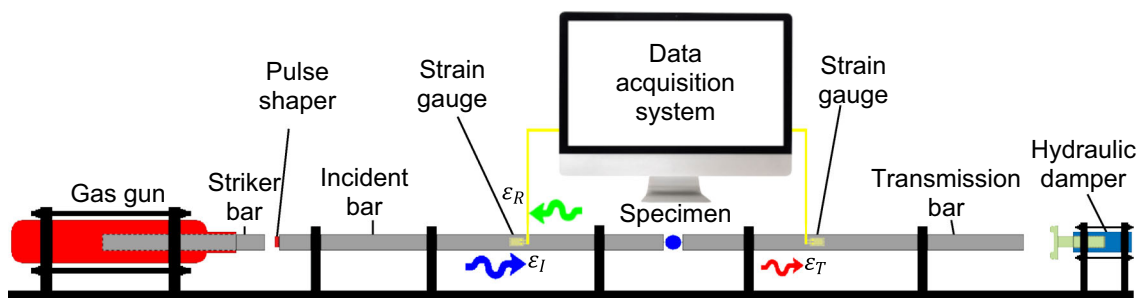


Fig. 1 Schematic view of the split Hopkinson pressure bar apparatus [34]

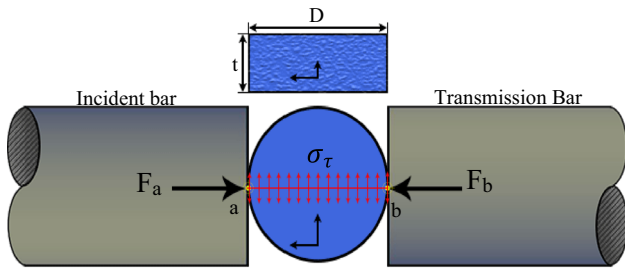


Fig. 3 Brazilian disk specimen in the SHPB test

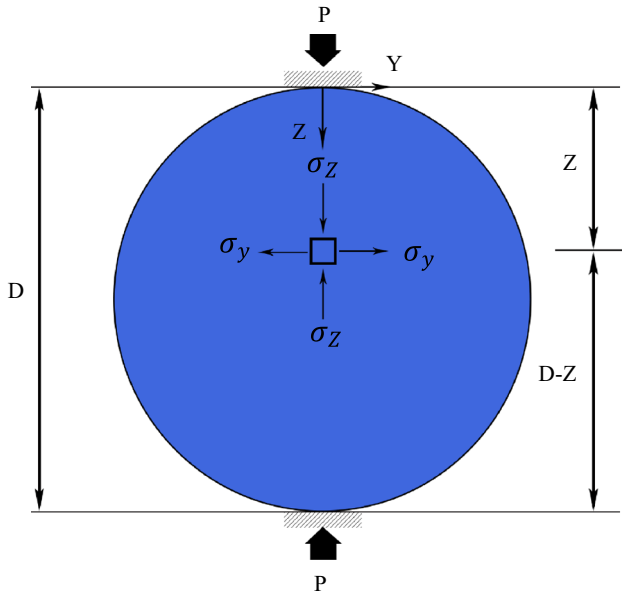


Fig. 4 Stress components in a Brazilian test

$$\dot{\sigma} = \frac{\sigma_{\tau_{max}}}{\tau'} \tag{6}$$

where $\sigma_{\tau_{max}}$ is the maximum tensile stress at the center of the specimen and τ' is the time delay between the start and the peak of the transmitted stress wave, and:

$$\dot{\epsilon} = \frac{\dot{\sigma}}{E_S} \tag{7}$$

where E_S is the Young’s modulus of the specimen.

An alternative and more accurate method for determination of stress rate is to consider all the stress components ($\sigma_x, \sigma_y, \sigma_z$) at the center of the specimen. For the plane stress situation, $\sigma_x = 0$ and σ_z stress component can be calculated [4] from the following equation (Fig. 4):

$$\sigma_z = -\frac{2P}{\pi Dt} \left[\frac{D^2}{z(D-z)} - 1 \right] \tag{8a}$$

Therefore, at the center of the specimen, we have:

$$\sigma_z = -\frac{6P}{\pi Dt} \tag{8b}$$

$$\sigma_y = \frac{2P}{\pi Dt} \tag{9}$$

The tensile strain at the specimen center is equal to:

$$\epsilon_y = \frac{1}{E_S} (\sigma_y - \nu\sigma_z - \nu\sigma_x) \tag{10}$$

Or

$$\epsilon = \epsilon_y = -\frac{1 + 3\nu}{E_S} \left[\frac{2EA}{\pi Dt} \epsilon_T \right] \tag{11}$$

where ν is the Poisson’s ratio of the rock. By taking derivative from both sides of Eq. (11), the strain rate at the center of the specimen can be obtained using the strain rate in the transmission bar.

3 Micromechanical Model

The SHPB test was simulated numerically by the CA3 program [35] which is a hybrid discrete–finite-element code for 3D simulation of geo-materials. The rock was modelled by the bonded particle system [33] which is a discrete element system whose elements are made of spherical particles. The spherical particles interact at the contact points by normal and shear springs. The normal and shear spring constants are shown by k_n and k_s , respectively. The contact points are assumed to have normal bond (n_b) and shear bond (s_b) to withstand the deviatoric stresses. A contact point can break in tension or shear if the applied force at the contact point exceeds the normal bond or shear bond. Following the failure of a contact point, it follows the coulomb frictional law with the friction coefficient μ . In summary, five micromechanical parameters are needed for interaction of spherical particles in the CA3 program (Fig. 5).

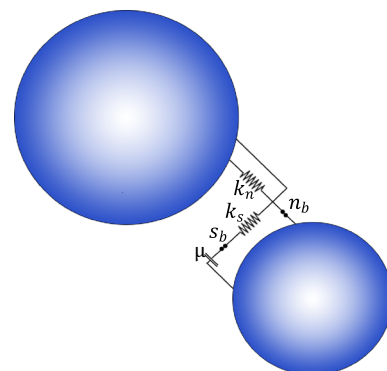


Fig. 5 Micromechanical elements for interaction of two spherical particles

Table 1 The macro-mechanical properties of the sandstone


	Compressive strength	Tensile strength	Elastic modulus	Poisson's ratio	Density
	(MPa)	(MPa)	(GPa)	-	(kg/m ³)
	122	9.9	27	0.15	2700

Table 2 The micro-mechanical parameters for the numerical specimen

$r_{particles}$	Radius of spherical particles (mm)	0.15–0.225
σ_0	Genesis pressure (GPa)	4.28
k_n	Normal spring stiffness (MN/m)	10.4
k_s	Shear spring stiffness (MN/m)	3.82
n_b	Normal bond (N)	0.9
s_b	Shear bond (N)	4.1
μ	Coefficient of friction of contact points	0.5

Table 3 The characteristics of the SHPB apparatus

Density of the bars (kg/m ³)	8100
Elastic modulus of the bars (GPa)	200
Poisson's ratio of the bars	0.3
Wave velocity along the bars (m/s)	4970
Incident bar length (mm)	1830
Transmission bar length (mm)	1218
Diameter of bars (mm)	12.7

While the contact bond model described by the five parameters k_n , k_s , n_b , s_b , and μ has been successful in simulating rock strength and its failure in static loading, it has shown difficulty in capturing strength enhancement in dynamic loading; inertia alone could not provide material rate dependency observed in the physical tests. To remedy this problem, Fakhimi et al. [34] proposed a phenomenological micromechanical model in which the contact bond strength increases with the increase in the relative velocity of the particles at the contact point:

$$n_b := n_b \times e^{\left(\frac{\beta'_n}{c_s} \times V_{nr}\right)} \tag{12}$$

$$s_b := s_b \times e^{\left(\frac{\beta'_s}{c_s} \times V_{sr}\right)} \tag{13}$$

where V_{nr} and V_{sr} are relative normal and shear velocities of the particles at their contact point, β'_n and β'_s are two dimensionless micromechanical constants called strength enhancement coefficients, and c_s is the wave speed in the rock specimen defined by:

$$c_s = \sqrt{\frac{E_s}{\rho_s}} \tag{14}$$

The sign := in Eqs. (12) and (13) means that the static values of the normal bond and shear bond on the right sides of the equations are replaced with the corresponding dynamic values on the left sides of those expressions in the dynamic analysis. Note that instead of β'_n and β'_s , in the previous publication [34], $\beta_n = \frac{\beta'_n}{c_s}$ and $\beta_s = \frac{\beta'_s}{c_s}$ were used which have the dimension of s/m. In the next sections of the paper, the results of numerical and experimental uniaxial compression tests are compared to justify the appropriateness of Eqs. (12) and (13), and then, the model is applied for some tensile Brazilian tests to reveal the usefulness of the model when tensile loading of a rock specimen is involved.

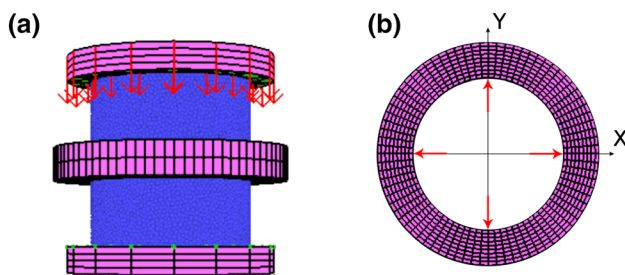


Fig. 6 Numerical uniaxial compression test

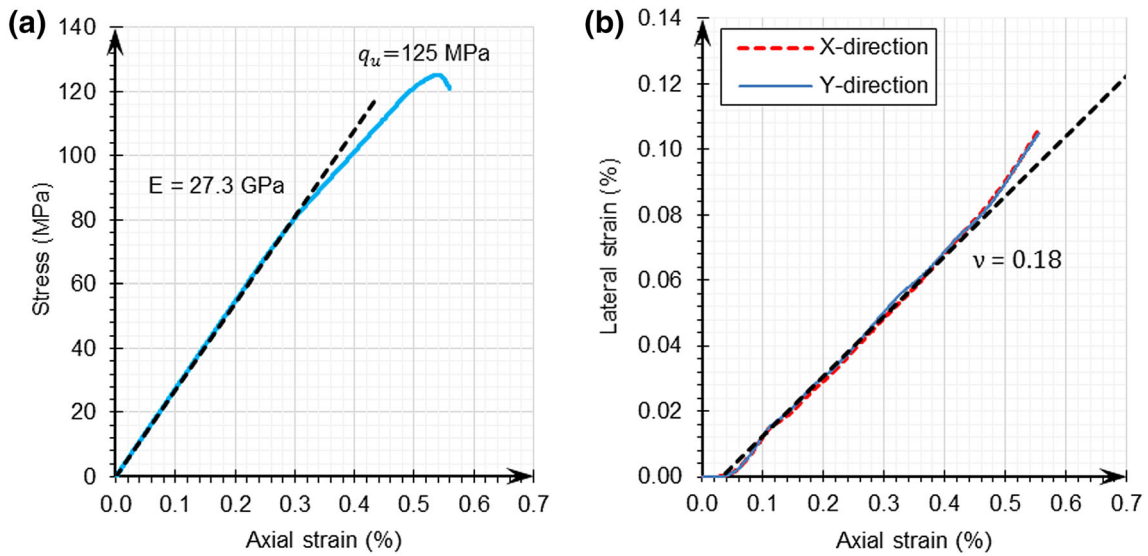


Fig. 7 Numerical uniaxial compression test result: **a** stress–axial strain curve, **b** lateral strain–axial strain curve

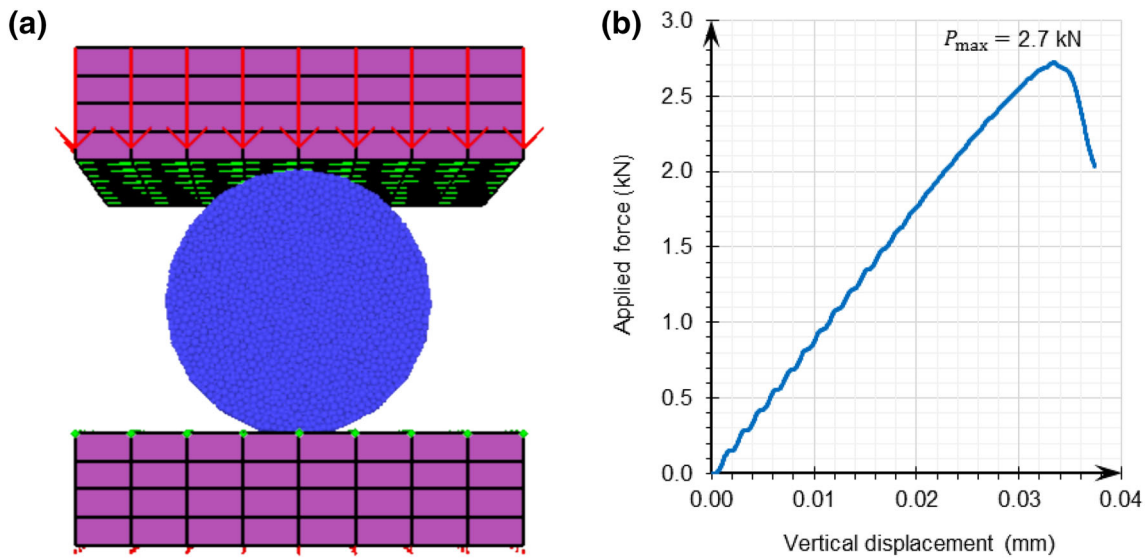


Fig. 8 **a** Brazilian tensile test setup and **b** load–displacement curve

Table 4 Comparison of the physical properties of sandstone and bonded particle model

Physical properties	Sandstone	Numerical simulation
Compressive strength (MPa)	122	125
Tensile strength (MPa)	9.9	10.7
Elastic modulus (GPa)	27	27.3
Poisson’s ratio	0.15	0.18

4 Bonded Particle Model

4.1 Calibration

In the bonded particle model, the micromechanical parameters (k_n, k_s, n_b, s_b and μ) must be calculated by the calibration procedure. To this end, the macroscopic rock physical properties need to be measured (Table 1), and then, by conducting numerical tests, the micromechanical properties are determined by the procedure such as the one discussed in [36] or by trial and error. Appropriate micro-properties are those that can reproduce the mechanical properties of rock.

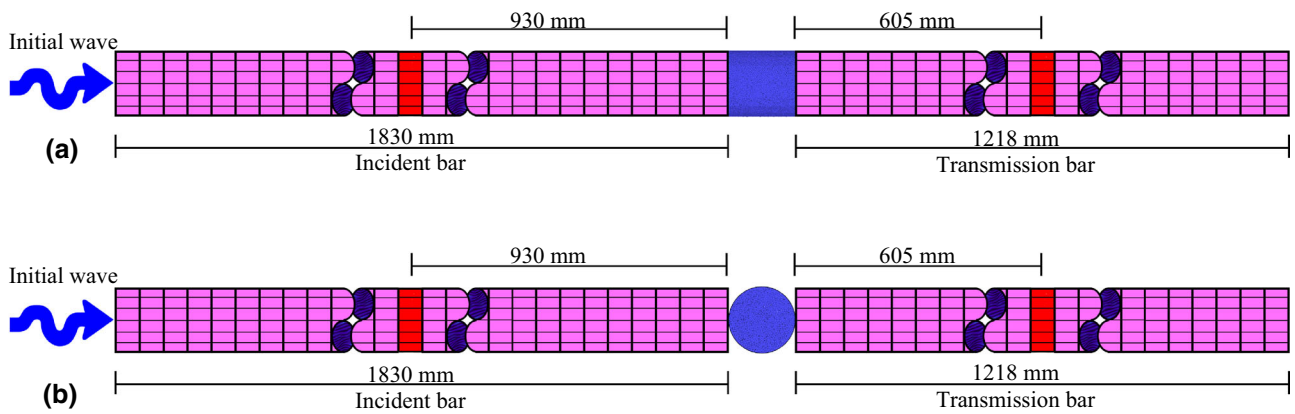


Fig. 9 a Uniaxial, b Brazilian, SHPB test setup. Red elements are to show the places where strain gauges are mounted in the physical test or stress is measured (recorded) in the numerical tests

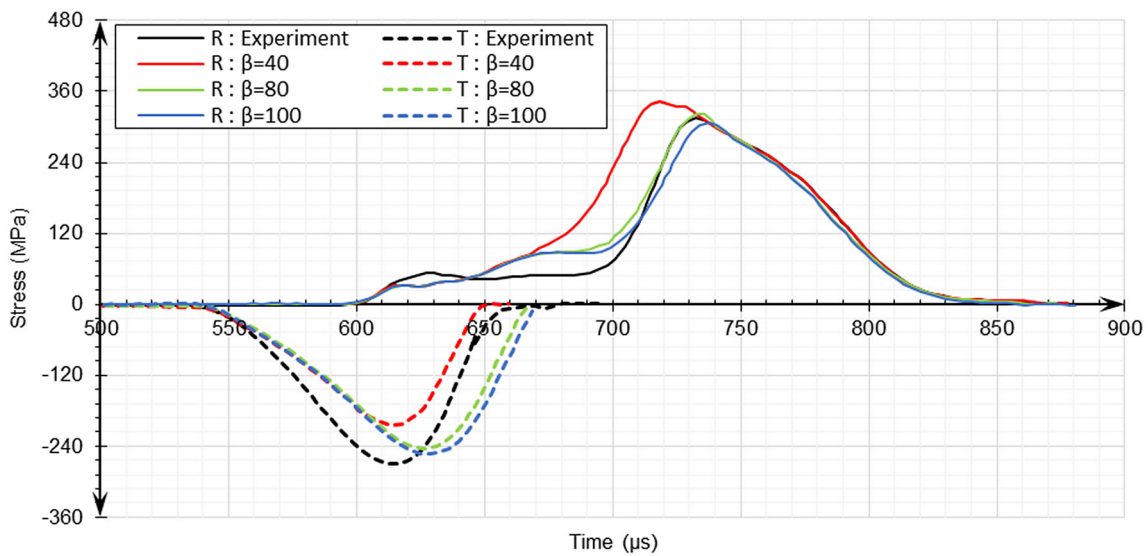


Fig. 10 Comparison between the numerical outputs with $\beta = 40 - 100 \frac{\text{s}}{\text{m}}$ ($\beta' = 12.7 \times 10^4, 25.4 \times 10^4$ and 31.8×10^4) and the experimental results in uniaxial compressive tests [34]. R and T stand for reflected and transmitted waves, respectively

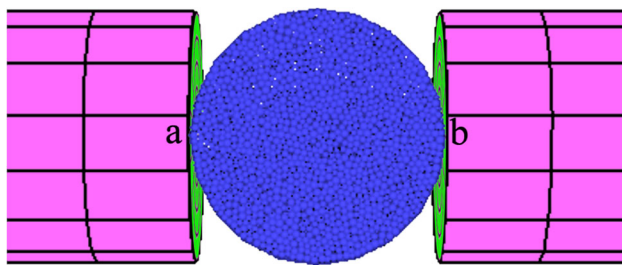


Fig. 11 Closed up view of the numerical specimen in the SHPB test

Following the procedure discussed in [36], the BPM calibration was successfully performed and the micro properties were obtained (Table 2). The radius of spherical particles in the BPM ranges from 0.15 to 0.225 mm with

Table 5 Time shifting of the waves

Wave	Distance (mm)	Time shifting (μs)
Incident wave	+ 930	+ 187.15
Reflected wave	- 930	- 187.15
Transmitted wave	- 605	- 120.74

the average value of 0.1875 mm. Consistent with that for the rock specimen, a density of 2700 kg/m^3 was considered for the particles.

The physical dimensions and properties of the Split Hopkinson bars [34] are reported in Table 3. A slenderness

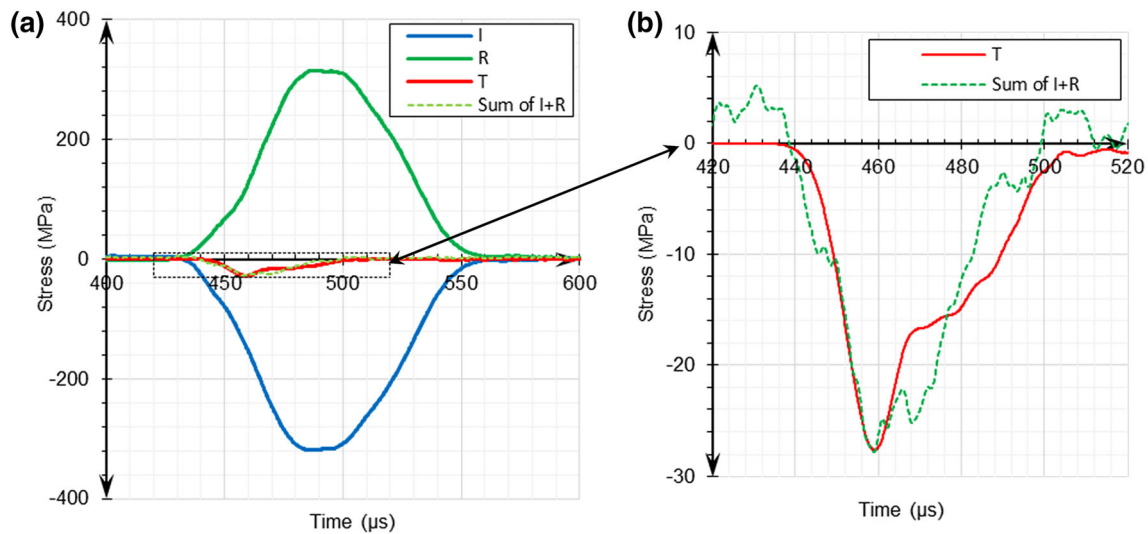


Fig. 12 **a** Shifted stress data in time to calculate the specimen ends forces; **b** dynamic equilibrium in the Brazilian test. I, R, and T stand for incident, reflected, and transmitted stress waves, respectively

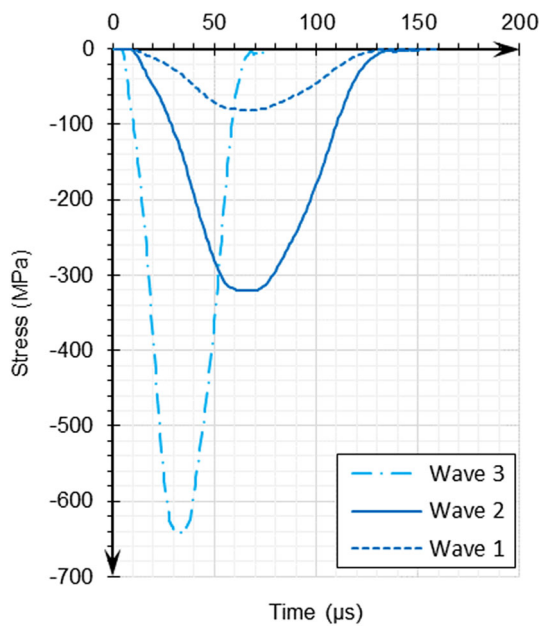


Fig. 13 Different incident waves considered in this study

ratio $t/D = 1$ [5] is considered for the specimen in this study. This means that for uniaxial compression and Brazilian tests, the specimen diameter is 12.7 mm (consistent with that in Table 3). Furthermore, the specimen length (in uniaxial compression) and specimen thickness (in Brazilian test) are 12.7 mm.

4.2 Calibration Verification

To verify the appropriateness of the calibrated model in mimicking the sandstone behavior, some static uniaxial compressive and Brazilian tests were performed. The

Table 6 Six different combinations of β'_n and β'_s coefficients used in this study

	$\beta'_n (\times 10^4)$	$\beta'_s (\times 10^4)$	$\beta_n (S/m)$	$\beta_s (S/m)$
1	0	0	0	0
2	12.7	12.7	40	40
3	25.4	25.4	80	80
4	31.8	31.8	100	100
5	31.8	159	100	500
6	159	31.8	500	100

prepared specimen for the uniaxial compression test is shown in Fig. 6. The finite-element ring in the middle of the specimen has a very low stiffness and is used to measure the lateral deformation of the bonded particle system. The numerical axial stress–axial strain curve is shown in Fig. 7a. Note that the elastic modulus (27.3 GPa) and the compressive strength (125 MPa) are in good agreement with the physical data reported in Table 1. The numerical lateral deformation data shown in Fig. 7 suggest a Poisson’s ratio of 0.18 which can be compared with that for the sandstone (Table 1).

The numerical Brazilian test setup is shown in Fig. 8a, while the load–displacement curve is demonstrated in Fig. 8b. The peak load from this test is 2.7 kN from which the material indirect tensile strength of 10.7 MPa is obtained. This value is closed to the actual tensile strength of the sandstone (Table 1). In summary, the numerical tests results confirm that the macroscopic physical properties of the sandstone can be closely reproduced (Table 4). This

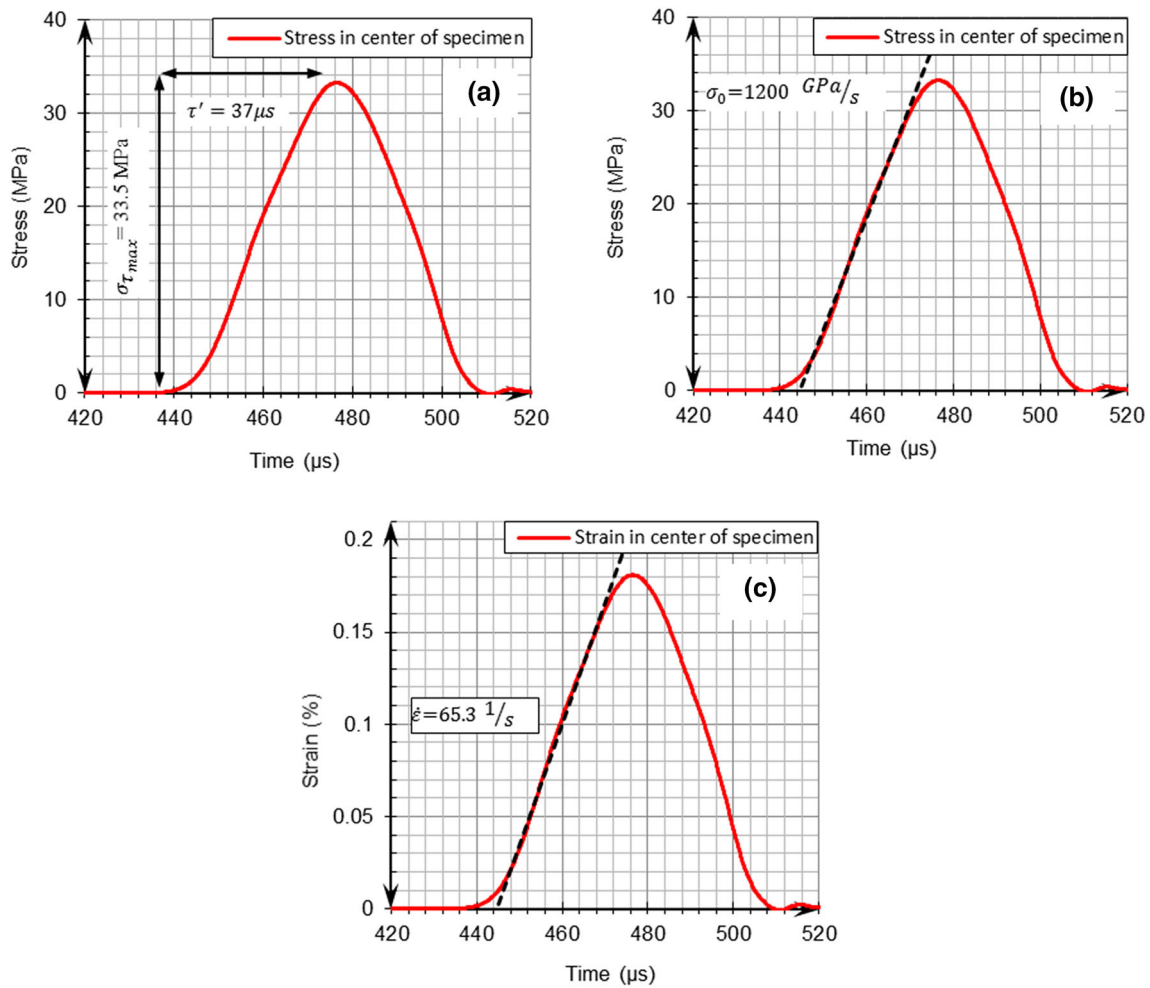


Fig. 14 Estimation of strain rate by a tensile stress in the specimen, b linear method, and c suggested method based on Eq. (11)

suggests that the micromechanical parameters of the bonded particle system (Table 2) are valid.

5 Numerical Simulation Of SHPB System

The incident and transmission bars were assumed to be linear elastic with properties reported in Table 3. The bars were discretized to finite elements. On the other hand, the cylindrical specimen (12.7 mm in length and 12.7 mm in diameter) was assumed to be made of bonded particles. The numerical SHPB test setup for the uniaxial compression test is shown in Fig. 9a. The incident wave as a stress wave is applied to the left end of the incident bar and propagates along the bar until it reaches the specimen. Part of the wave is transmitted through the specimen and the transmission bar, while the other part is reflected back in the incident bar due to the impedance mismatch of the steel bar and the rock specimen. The stress (or strain) at the locations shown in red in Fig. 9 is measured during the

numerical test. The test setup in Fig. 9 is similar to that reported in [34] and similar input wave as that in [34] was used in our analysis.

The numerical test results of the reflected and transmitted waves for three different cases of $\beta = \beta_n = \beta_s = 40, 80, 100 \text{ s/m}$ (or in dimensionless form: $\beta' = \beta'_n = \beta'_s = 12.7 \times 10^4, 25.4 \times 10^4$ and 31.8×10^4) are shown in Fig. 10. Notice how with a value of $\beta' = 25$ to 32×10^4 , not only the peak values but also the shape of the transmitted and reflect experimental waves can be reproduced numerically, suggesting that Eqs. (12) and (13) are capturing the mechanical behavior of the material realistically.

To study the performance of the model in the indirect tensile test, the SHPB test setup of Fig. 9b was used. In a SHPB test, dynamic equilibrium of the specimen needs to be satisfied. To this end, the incident, reflected, and transmitted waves were shifted in time to help to calculate the specimen ends forces (ends a and b in Fig. 11). Time shifting is calculated using the distance of strain gauges

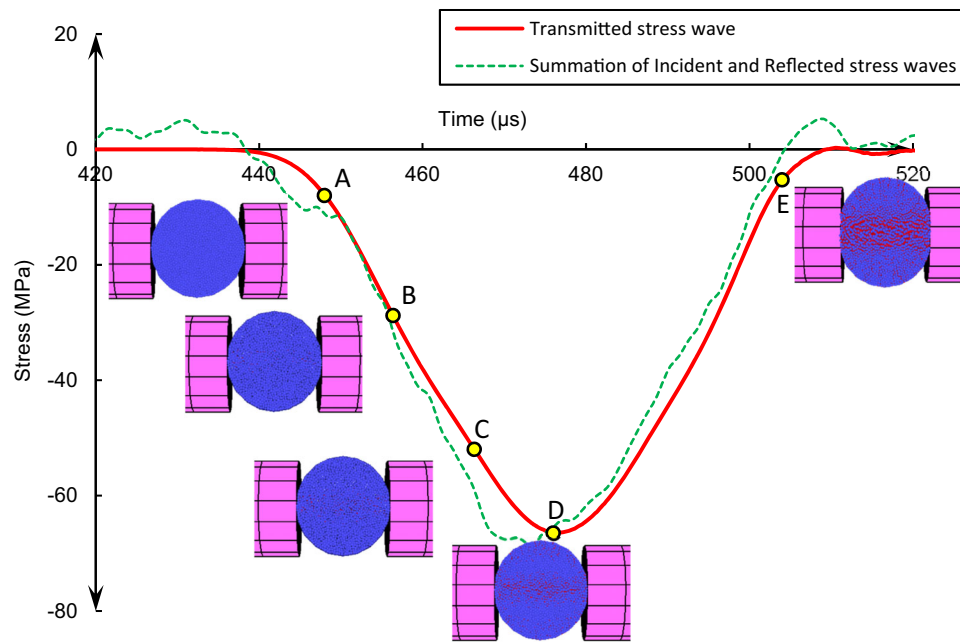


Fig. 15 Dynamic equilibrium and micro-cracking processes in the numerical specimen

from the specimen ends (Fig. 9 and Table 5). To assure dynamic equilibrium, the summation of incident and reflected waves must be equal to the transmitted wave. As it can be realized from Fig. 12, in our numerical simulation, dynamic equilibrium has been achieved reasonably well.

In addition to the incident wave discussed above, two more incident waves were considered in our study to scrutinize the role of strain or stress rate on the strength enhancement. All the three incident waves are depicted in Fig. 13. These incident waves together with different values of micromechanical constants β'_n and β'_s (Table 6) were used, and several numerical exercises were conducted. Three different methods were applied to measure the strain rate of the specimen. Sample calculation for the incident wave 2 (Fig. 13) with $\beta'_n = \beta'_s = 31.8 \times 10^4$ is reported here. In the first method, Eqs. (4) and (5) are used to calculate the stress at the specimen center and, therefore, from Fig. 14a, with the value of the stress rate $\dot{\sigma} = \frac{\sigma_{rmax}}{\tau} = \frac{33.5 \text{ MPa}}{37 \mu\text{s}} = 905 \text{ GPa/s}$, the strain rate is calculated as $\dot{\epsilon} = \frac{\dot{\sigma}}{E_s} = \frac{905}{27.3} = 33.1 \text{ 1/s}$. In the second method, the slope of linear part of Fig. 14b is utilized to measure the stress rate (1200 GPa/s) and the strain rate is calculated as $\dot{\epsilon} = \frac{\dot{\sigma}}{E_s} = \frac{1200}{27.3} = 44 \text{ 1/s}$. The strain rate (Fig. 14c) is calculated from Eq. (11) in the third method ($\dot{\epsilon} = 65.31/\text{s}$).

The micro-cracking processes for the specimen subjected to the wave 2 and with the micro-parameters $\beta'_n = 31.8 \times 10^4$, $\beta'_s = 31.8 \times 10^4$ are shown in Fig. 15. Notice that as expected, the cracking are mostly along the

specimen diameter and parallel to the direction of applied load. In the same figure, the summation of incident and reflected stress waves is compared with the transmitted stress, confirming that the necessary condition for dynamic equilibrium of the specimen has been fulfilled.

The results of the conducted numerical exercises for different incident waves and different micromechanical constants β'_n and β'_s are reported in Table 7. Notice that different approaches used to measure the strain rate do not end up to the same values. Furthermore, as expected, with the increase in the strength enhancement micromechanical constants, greater rock strength is obtained. It is interesting to note that the influence of β'_n on rock strength seems to be more important compared to that of β'_s . This fact can be realized by comparing the rock strength for the last two tests (under incident wave 1) reported in Table 7. The reason for this observation is that most of the induced micro-cracks at the contact points of the bonded particles are tensile crack (shown in red in Fig. 15) and, therefore, β'_n which is involved with the tensile strength of contact points should play a more important role compared to the β'_s parameter. It should be mentioned that the DIF in the last column of Table 7 stands for the dynamic increase factor which is simply the ratio of dynamic strength to the static value.

The transmitted and reflected wave forms due to the applied incident waves 1, 2, and 3 are shown in Fig. 16. Note that by changing the strength enhancement micromechanical constants, the wave form can be modified. This procedure was followed in the work by Fakhimi

Table 7 Numerical test results for dynamic increase factor (DIF)

	Strength enhancement coefficient ($\times 10^4$)	Dynamic tensile strength (MPa)	Strain rate ($1/s$)			DIF
			(1)*	(2)**	(3)***	
Wave 1	$\beta'_n = 0, \beta'_s = 0$	11.8	12.3	31.5	45.7	1.1
	$\beta'_n = 12.7, \beta'_s = 12.7$	16.5	15.9	37.3	55.4	1.5
	$\beta'_n = 25.4, \beta'_s = 25.4$	18.2	16.3	38.7	57.6	1.7
	$\beta'_n = 31.8, \beta'_s = 31.8$	18.9	16.9	40.7	60.5	1.75
	$\beta'_n = 31.8, \beta'_s = 159$	19	17.3	40.7	60.5	1.76
	$\beta'_n = 159, \beta'_s = 31.8$	2.3	23	47.2	70.1	2.3
Wave 2	$\beta'_n = 0, \beta'_s = 0$	13.8	25.3	29.8	57.6	1.3
	$\beta'_n = 12.7, \beta'_s = 12.7$	24.4	27.9	42.2	62.7	2.3
	$\beta'_n = 25.4, \beta'_s = 25.4$	30.7	29.6	42.8	63.6	2.9
	$\beta'_n = 31.8, \beta'_s = 31.8$	33.5	33.1	44	65.3	3.1
	$\beta'_n = 31.8, \beta'_s = 159$	36.7	31.8	43.3	64.3	3.4
	$\beta'_n = 159, \beta'_s = 159$	62.9	51.2	63.6	94.4	5.8
Wave 3	$\beta'_n = 0, \beta'_s = 0$	23.9	62.5	135.2	201	2.2
	$\beta'_n = 12.7, \beta'_s = 12.7$	70	142.5	391	581	6.5
	$\beta'_n = 25.4, \beta'_s = 25.4$	85.1	156	454	676	7.9
	$\beta'_n = 31.8, \beta'_s = 31.8$	90.4	166	476	707	8.4
	$\beta'_n = 31.8, \beta'_s = 159$	96	176	485	710	9
	$\beta'_n = 159, \beta'_s = 159$	140	256	635	950	13

*First method; ^bsecond method; ^cthird method, for calculation of strain rate

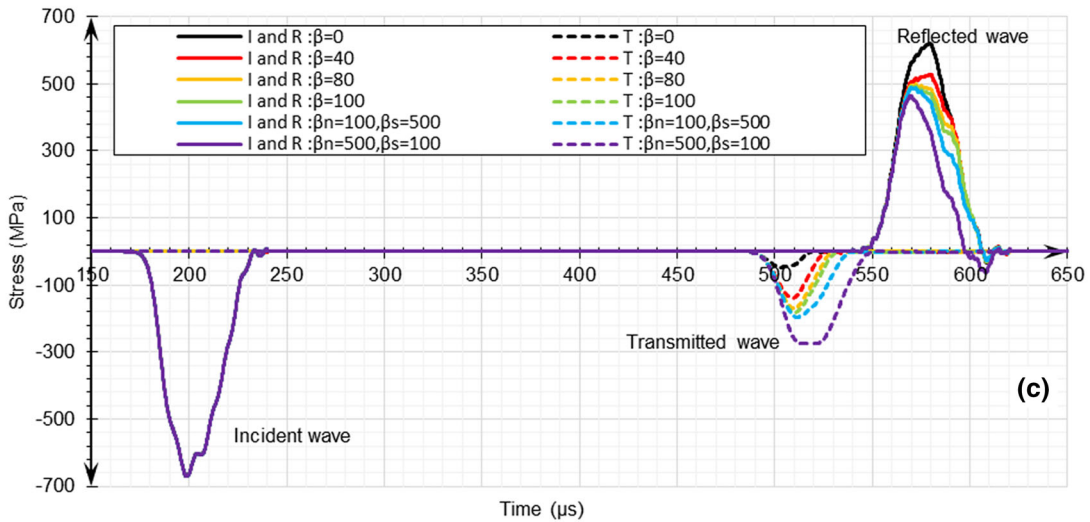
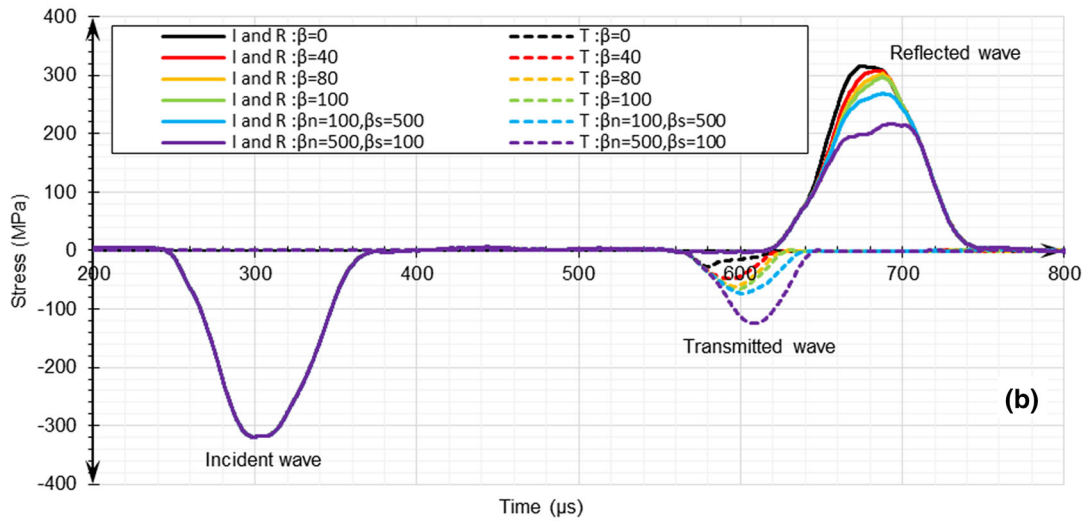
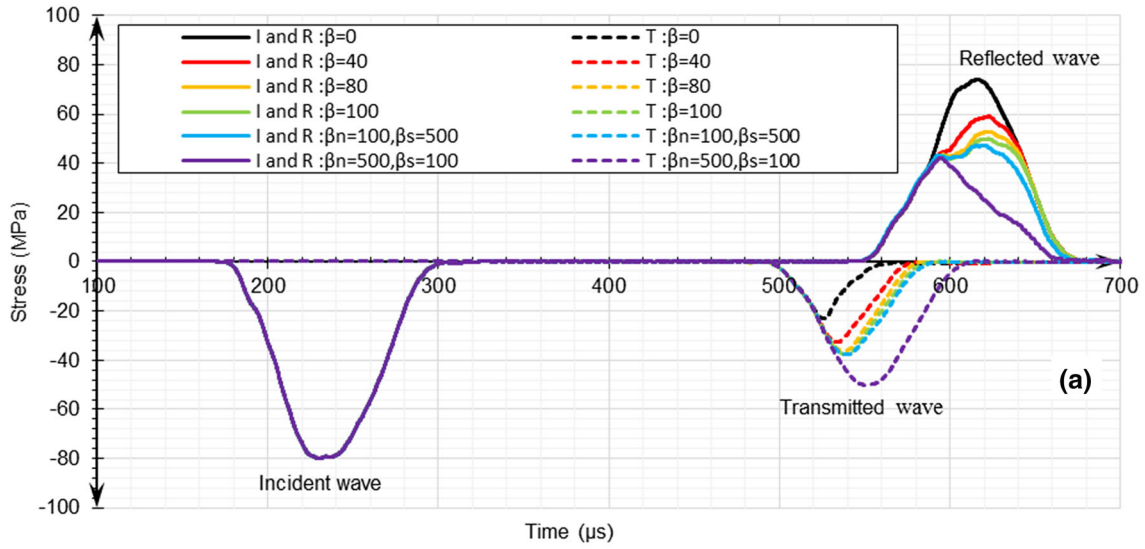
et al. [34] for uniaxial compression tests on blue sandstone specimens, and it was shown that the numerical and physical wave forms can be closely matched if the micromechanical constants $\beta'_n = \beta'_s = 12.7-31.8(\times 10^4)$ or $\beta_n = \beta_s = 40-100$ s/m are used (Fig. 10).

6 Validation

The work in [34] suggests that Eqs. (12) and (13) are capable of reproducing strength enhancement of sandstone under uniaxial compression dynamic loading. To check validity of these equations for tensile loading, the results of our numerical analysis are compared with the physical tests data in Fig. 17. The experimental data are for sandstone specimens and are reported in [6]. The numerical data for $\beta = \beta_n = \beta_s = 0$ in Fig. 17 clearly underestimate the

physical values, meaning that inertia alone has not been capable enough to capture the material behavior under high strain rate loading. On the other hand, with $\beta = \beta_n = \beta_s = 40 - 100$ s/m, the physical rate dependency of sandstone strength can be reasonably well captured by the proposed phenomenological model. It is interesting to realize that the same values of β were also used in [34] and were able to reproduce the sandstone strength enhancement consistent with the physical observation. In summary, it appears that with the same values of micromechanical strength enhancement parameters, both the compressive and tensile strength of sandstone specimens can be reasonably well simulated.

DIF values for high strength concrete under tensile and compressive loading were measured and are reported in Fig. 18 [4]. From this figure, it appears that quasi-brittle materials such as concrete demonstrate different rate



◀ **Fig. 16** The effect of the applied enhancement coefficient β (s/m) (or β') on the response and strength of the specimen using the input corresponding to the incident wave **a** 1, **b** 2, and **c** 3

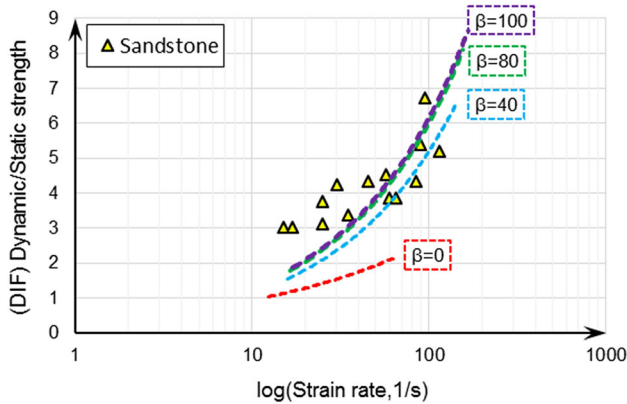


Fig. 17 Comparison of physical and numerical DIF values. The physical data for the sandstone are from [6]

dependency behaviour under compression and tension; they are more sensitive to the applied strain rate in tension. In Fig. 18, the data points from physical and numerical tests for the blue sandstone are shown as well. The figure clearly indicates that the proposed micromechanical model shows non-identical rate dependency in tension and compression. More physical and numerical data are needed for further elaboration on this finding.

Lu et al. [37] performed tensile tests on different rocks and presented a general diagram of the dynamic increase factor versus the loading rate (Fig. 19). The results of the numerical tests of this study for $\beta = \beta_n = \beta_s = 40 - 100$ s/m are shown in Fig. 19 too. Considering the scatter of the physical tests data, this figure confirms that for the assumed values of the micromechanical enhancement coefficients, the general trend of rock strength rate dependency can be captured with reasonable accuracy within the framework of the proposed micromechanical model.

7 Conclusion

In this investigation, numerical Split Hopkinson pressure bar (SHPB) Brazilian tensile tests under high strain rates were conducted. CA3 which is a hybrid-bonded particle-finite-element program for 3D simulation of geomaterials was used in the study. The rock was modelled by a bonded particle system while the incident and transmitted bars were simulated by finite-element method. The numerical results suggest that a simple contact bond model for the bonded particle system is not able to reproduce reasonable results for the dynamic situation. For this reason, a micromechanical model which allows the bond strength between the particles to increase in proportion to the relative velocity of the particles is suggested. It appears that the proposed model can help to match the numerical

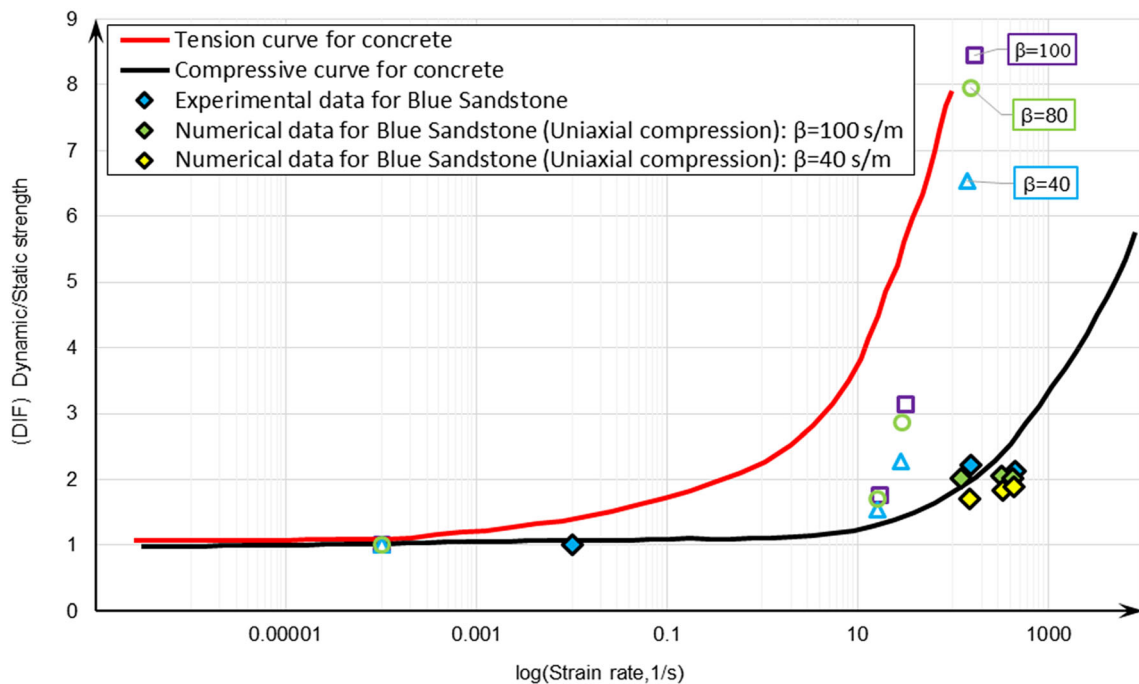


Fig. 18 Comparison of DIF values from [4] and our study. The hollow and filled symbols are the results of tensile and compressive loading, respectively

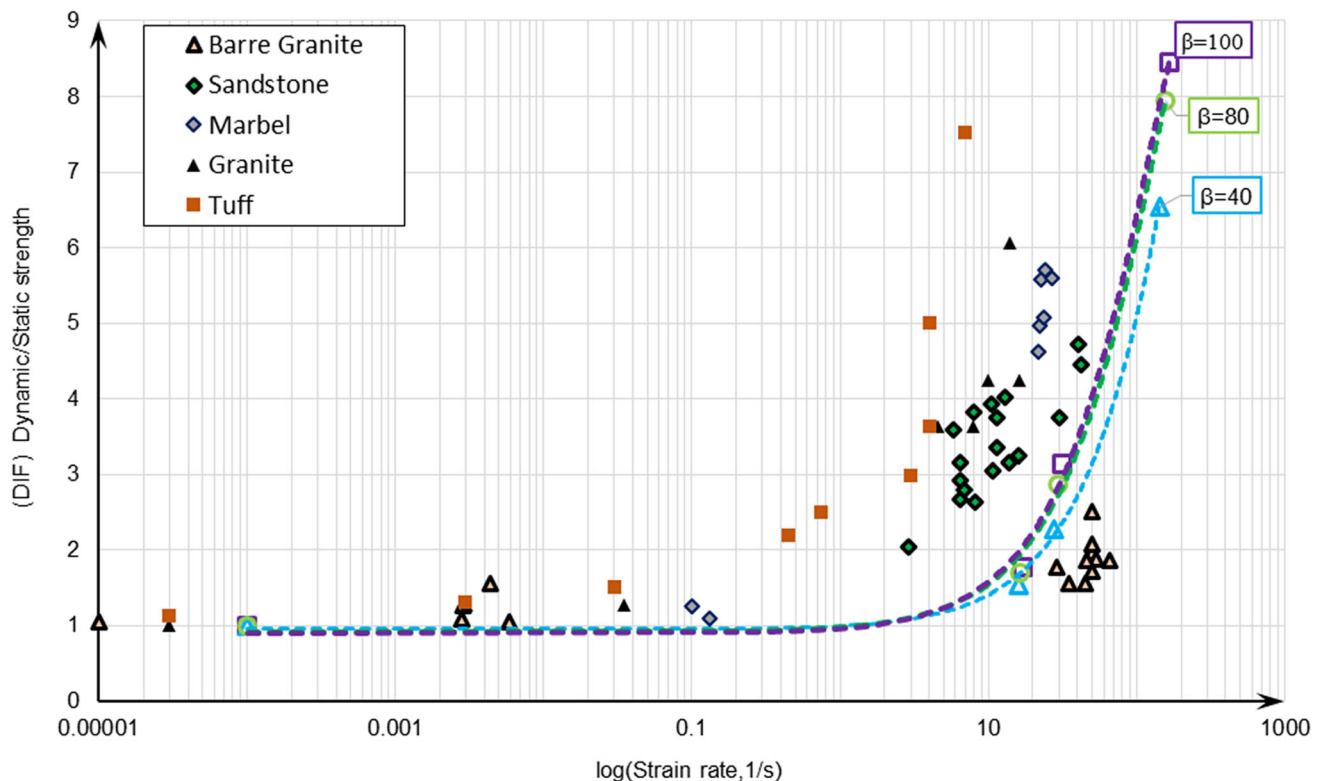


Fig. 19 DIF in tensile tests versus strain rate for different rock specimen [37]. The numerical tests results of this study are shown with dashed lines

reflected and transmitted wave forms with those of the physical data closely. Furthermore, the model can reasonably well reproduce physical dynamic increase factor values reported in the literature.

Acknowledgements The third author acknowledges the support he received in developing CA3 program during his years of service at New Mexico Tech.

References

- Brown ET (1981) Rock characterization testing and monitoring. ISRM suggested methods. Rock Charact. Test. Monit. ISRM Suggest. methods
- Xia K, Yao W (2015) Dynamic rock tests using split Hopkinson (Kolsky) bar system—A review. *J Rock Mech Geotech Eng* 7:27–59. <https://doi.org/10.1016/j.jrmge.2014.07.008>
- Lindholm US (1964) Some experiments with the split hopkinson pressure bar*. *J Mech Phys Solids* 12:317–335. [https://doi.org/10.1016/0022-5096\(64\)90028-6](https://doi.org/10.1016/0022-5096(64)90028-6)
- Hughes ML, Tedesco JW, Ross CA (1993) Numerical analysis of high strain rate splitting-tensile tests. *Comput Struct* 47:653–671. [https://doi.org/10.1016/0045-7949\(93\)90349-I](https://doi.org/10.1016/0045-7949(93)90349-I)
- Dai F, Huang S, Xia K, Tan Z (2010) Some fundamental issues in dynamic compression and tension tests of rocks using Split Hopkinson Pressure Bar. *Rock Mech Rock Eng* 43:657–666. <https://doi.org/10.1007/s00603-010-0091-8>
- Das S (2016) A strain-rate dependent tensile damage model for brittle materials under impact loading. Ph.D. Thesis, University of Sydney
- Li X, Mao H, Xu K, Miao C (2018) A SHPB experimental study on dynamic mechanical property of high-damping rubber. *Shock Vib* 2018:1–10. <https://doi.org/10.1155/2018/3128268>
- Ai D, Zhao Y, Wang Q, Li C (2020) Crack propagation and dynamic properties of coal under SHPB impact loading: experimental investigation and numerical simulation. *Theor Appl Fract Mech* 105:102393. <https://doi.org/10.1016/j.tafmec.2019.102393>
- Feng W, Liu F, Yang F et al (2019) Experimental study on the effect of strain rates on the dynamic flexural properties of rubber concrete. *Constr Build Mater* 224:408–419. <https://doi.org/10.1016/j.conbuildmat.2019.07.084>
- Gálvez F, Rodríguez J, Sánchez V (1997) Tensile strength measurements of ceramic materials at high rates of strain. *Le J Phys IV* 07:C3-151–C3-156. <https://doi.org/10.1051/jp4:1997328>
- Tedesco JW, Ross CA, McGill PB, O'Neil BP (1991) Numerical analysis of high strain rate concrete direct tension tests. *Comput Struct* 40:313–327. [https://doi.org/10.1016/0045-7949\(91\)90357-R](https://doi.org/10.1016/0045-7949(91)90357-R)
- Meng H, Li QM (2003) Correlation between the accuracy of a SHPB test and the stress uniformity based on numerical experiments. *Int J Impact Eng* 28:537–555. [https://doi.org/10.1016/S0734-743X\(02\)00073-8](https://doi.org/10.1016/S0734-743X(02)00073-8)
- Zhong WZ, Rusinek A, Jankowiak T et al (2015) Influence of interfacial friction and specimen configuration in Split Hopkinson Pressure Bar system. *Tribol Int* 90:1–14. <https://doi.org/10.1016/J.TRIBOINT.2015.04.002>
- Binesh SM, Eslami-Feizabad E, Rahmani R (2018) Discrete element modeling of drained triaxial test: flexible and rigid lateral

- boundaries. *Int J Civ Eng* 16:1463–1474. <https://doi.org/10.1007/s40999-018-0293-0>
15. Wang W, Sun S, Le H et al (2019) Experimental and numerical study on failure modes and shear strength parameters of rock-like specimens containing two infilled flaws. *Int J Civ Eng* 17:1895–1908. <https://doi.org/10.1007/s40999-019-00449-8>
 16. Hoormazdi G, Küpferle J, Röttger A et al (2019) a concept for the estimation of soil-tool abrasive wear using ASTM-G65 test data. *Int J Civ Eng* 17:103–111. <https://doi.org/10.1007/s40999-018-0333-9>
 17. Cundall PA (1971) A computer model for simulating progressive, large-scale movement in blocky rock system. In: *Proc Int Symp Rock Mech* 1971
 18. Rojek J, Oñate E, Labra C, Kargl H (2011) Discrete element simulation of rock cutting. *Int J Rock Mech Min Sci* 48:996–1010. <https://doi.org/10.1016/j.ijrmms.2011.06.003>
 19. Rojek J (2014) Discrete element thermomechanical modelling of rock cutting with valuation of tool wear. *Comput Part Mech* 1:71–84. <https://doi.org/10.1007/s40571-014-0008-5>
 20. Fakhimi A, Wan F (2016) Discrete element modeling of the process zone shape in mode I fracture at peak load and in post-peak regime. *Int J Rock Mech Min Sci* 85:119–128. <https://doi.org/10.1016/j.IJRMMS.2016.03.014>
 21. Tarokh A, Kao C-S, Fakhimi A, Labuz JF (2016) Insights on surface spalling of rock. *Comput Part Mech* 3:391–405. <https://doi.org/10.1007/s40571-016-0108-5>
 22. Lanari M, Fakhimi A (2015) Numerical study of contributions of shock wave and gas penetration toward induced rock damage during blasting. *Comput Part Mech* 2:197–208. <https://doi.org/10.1007/s40571-015-0053-8>
 23. Fakhimi A, Riedel JJ, Labuz JF (2006) Shear banding in sandstone: physical and numerical Studies. *Int J Geomech* 6:185–194. [https://doi.org/10.1061/\(ASCE\)1532-3641\(2006\)6:3\(185\)](https://doi.org/10.1061/(ASCE)1532-3641(2006)6:3(185))
 24. Brara A, Camborde F, Klepaczko JR, Mariotti C (2001) Experimental and numerical study of concrete at high strain rates in tension. *Mech Mater* 33:33–45. [https://doi.org/10.1016/S0167-6636\(00\)00035-1](https://doi.org/10.1016/S0167-6636(00)00035-1)
 25. Li X, Zou Y, Zhou Z (2014) Numerical Simulation of the Rock SHPB Test with a Special Shape Striker Based on the Discrete Element Method. *Rock Mech Rock Eng* 47:1693–1709. <https://doi.org/10.1007/s00603-013-0484-6>
 26. Yin T, Zhang S, Li X, Bai L (2018) A numerical estimate method of dynamic fracture initiation toughness of rock under high temperature. *Eng Fract Mech* 204:87–102. <https://doi.org/10.1016/j.engfracmech.2018.09.034>
 27. Du H, Dai F, Xu Y et al (2020) Mechanical responses and failure mechanism of hydrostatically pressurized rocks under combined compression-shear impacting. *Int J Mech Sci* 165:105219. <https://doi.org/10.1016/j.ijmecsci.2019.105219>
 28. Mahabadi OK, Cottrell BE, Grasselli G (2010) An example of realistic modelling of rock dynamics problems: FEM/DEM simulation of dynamic Brazilian test on barre granite. *Rock Mech Rock Eng* 43:707–716. <https://doi.org/10.1007/s00603-010-0092-7>
 29. Munjiza A (2004) *The combined finite-discrete element method*, 1st edn. Wiley, Chichester
 30. Rougier E, Knight EE, Broome ST et al (2014) Validation of a three-dimensional finite-discrete element method using experimental results of the Split Hopkinson Pressure Bar test. *Int J Rock Mech Min Sci* 70:101–108. <https://doi.org/10.1016/j.ijrmms.2014.03.011>
 31. Osthus D, Godinez HC, Rougier E, Srinivasan G (2018) Calibrating the stress-time curve of a combined finite-discrete element method to a Split Hopkinson Pressure Bar experiment. *Int J Rock Mech Min Sci* 106:278–288. <https://doi.org/10.1016/j.ijrmms.2018.03.016>
 32. O’Sullivan C (2011) *Particulate discrete element modelling: a geomechanics perspective*. CRC Press, Boca Raton
 33. Cundall PA, Strack ODL (1979) A discrete numerical model for granular assemblies. *Géotechnique* 29:47–65. <https://doi.org/10.1680/geot.1979.29.1.47>
 34. Fakhimi A, Azhdari P, Kimberley J (2018) Physical and numerical evaluation of rock strength in Split Hopkinson Pressure Bar testing. *Comput Geotech* 102:1–11. <https://doi.org/10.1016/j.compgeo.2018.05.009>
 35. Fakhimi A (2009) A hybrid discrete–finite element model for numerical simulation of geomaterials. *Comput Geotech* 36:386–395. <https://doi.org/10.1016/j.compgeo.2008.05.004>
 36. Fakhimi A, Villegas T (2007) Application of dimensional analysis in calibration of a discrete element model for rock deformation and fracture. *Rock Mech Rock Eng* 40:193–211. <https://doi.org/10.1007/s00603-006-0095-6>
 37. Lu YBB, Li QMM, Ma GWW (2010) Numerical investigation of the dynamic compressive strength of rocks based on split Hopkinson pressure bar tests. *Int J Rock Mech Min Sci* 47:829–838. <https://doi.org/10.1016/j.ijrmms.2010.03.013>